# Upgrade of the KWS-2 High-Intensity / Extended Q-range SANS Diffractometer of JCNS for Soft-Matter and Biophysics: in-situ SEC, controlled in-situ RH/T variation and WANS detection

**Jia-Jhen Kang.[a] Ralf Biehl.[b] Georg Brandl. [a] Helmut Korb. [a] Kimio Yoshimura. [c] Vladimir Ossovyi. [a] Andreas Nebel. [a] Jacqueline Lippertz. [d] Ralf Engels. [e] Günter Kemmerling. [e] Alexander Zaft. [a] Hiroki Iwase. [f] Hiroshi Arima-Osonoi. [g] Shin-ichi Takata. [h] Alexander Weber. [a] Simon Staringer. [a] Baohu Wu. [a] Yue Zhao. [c] Stefan Mattauch. [a] Aurel Radulescu. [a]***

[a] Jülich Centre for Neutron Science (JCNS) at Heinz Maier-Leibnitz Zentrum (MLZ), Forschungszentrum Jülich GmbH, 85748 Garching, Germany

[b] Jülich Centre for Neutron Science (JCNS-1) & Institute of Biological Information Processing (IBI-8), Forschungszentrum Jülich GmbH, 52425 Jülich, Germany

[c] Department of Advanced Functional Material Research, Takasaki Institute for Advanced Quantum Science, National Institutes for Quantum Science and Technology (QST), Takasaki, 370-1292, Japan

[d] Peter Grünberg Institute (PGI) & Jülich Centre for Neutron Science (JCNS), Forschungszentrum Jülich GmbH, 52425 Jülich, Germany

[e] Jülich Centre for Neutron Science (JCNS-2), Forschungszentrum Jülich GmbH, 52425 Jülich, Germany

[f] Neutron Science and Technology Centre, Comprehensive Research, Organization for Science and Society CROSS, Tokai, 319-1106, Japan

[g] Institute for Integrated Radiation and Nuclear Science, Kyoto University 2, Osaka 590-0494, Japan

[h] Materials and Life Science Division, Japan Proton Accelerator Complex J-PARC, Tokai, 319-1195, Japan

* a.radulescu@fz-juelich.de

**Synopsis** Upgrades at KWS-2 SANS diffractometer for an optimal sample quality for biological systems (in-beam SEC complementarity), a controlled humidity and temperature on ionic conductive samples and biological membranes and a diffraction capability (WANS) are reported.

**Abstract** The KWS-2 SANS diffractometer operated by Jülich Centre for Neutron Science at Heinz Maier-Leibnitz Zentrum, Garching, Germany, is dedicated to the investigation of mesoscopic multi-scale structures and structural changes due to rapid kinetic processes in soft condensed matter and biophysical systems. Following requests from the user community, it has been repeatedly upgraded with respect to the most important methodological parameters of an instrument of this type, namely the intensity on the sample, the instrumental resolution and the minimum scattering variable $Q_{min}$. Here we report on further specific improvements to the sample environment and detection capabilities that have

just been completed or are being implemented to improve the performance of the instrument for specific scientific applications. A complementary size exclusion chromatography (SEC) for in situ protein purification was developed and optimized at KWS-2 to provide the instrument with biological samples of controlled quality. The instrument is also currently being equipped with a diffraction capability - a Wide Angle Neutron Scattering (WANS) detector - which will allow it to bridge the atomic and mesoscale, benefiting from the instrument's adjustable resolution down to $\Delta\lambda/\lambda = 2\%$. For controlled relative humidity (RH) and temperature on ionic conductive samples for energy applications or biomembranes for biophysical and health applications, a precise dew point generator has recently been characterized and commissioned, offering great versatility in varying the contrast in-situ in the beam on hydrated samples.

**Keywords: SANS; WANS; SEC-SANS; semicrystalline polymers**

## 1. Introduction

The small-angle neutron diffractometer KWS-2 (Radulescu et al., 2012a) operated by the Jülich Centre for Neutron Science (JCNS) at the Heinz Maier-Leibnitz Zentrum (MLZ), Garching, Germany, is a high throughput instrument dedicated to the investigation of mesoscopic multi-scale structures and structural changes in soft condensed matter and biophysical systems. The instrument currently enables a broad Q range to be explored, between $2.0 \times 10^{-4}$ and 1.0 $Å^{-1}$, and offers high neutron intensities with MHz detection capabilities (Houston et al., 2018) and adjustable experimental resolutions (Radulescu et al., 2015a) in continuous or TOF mode based on the instrument's optimised neutron guide system (Radulescu et al. 2012b), versatile velocity selector, fast detection electronics for the main $^3$He detector and main double-disc chopper. A secondary single disc chopper (Balacescu et al., 2020) enables background reduction by facilitating the discarding of inelastically scattered neutrons from hydrogenated samples. The wide Q range is covered by the combination of the pinhole mode with variable wavelength $\lambda$ between 2.8 Å and 20 Å and a detection distance $L_D$ between 1.5 m and 20 m after the sample and the focussing mode with $MgF_2$ parabolic lenses and a secondary high-resolution detector (Radulescu et al., 2012a).

In this manuscript, we report recently accomplished and ongoing upgrades to the sample environment and detection capabilities at KWS-2 as follows: i) for a desired sample quality in beam while working with biophysical systems, the newly installed size-exclusion chromatography (SEC) complementarity provides the instrument with possibility of in-beam

selection of the right species of biological molecules to be investigated with neutrons while separating the undesired ones such aggregates or impurities before reaching the neutron sample cuvette; ii) to bridge the atomic and mesoscale structures, diffraction capabilities are just in commissioning that will provide opportunity for a complete analysis of multiple structural levels systems such as semi-crystalline polymers by covering an extend length scale from Ångstroms to micrometers at the same instrument while using the same sample and sample environment equipment; iii) to provide the instrument with the suitable sample environment conditions for allowing significant progress in the field of proton and anion exchange membranes and contribute to the replacement of hazardous fluorine containing membranes such Nafion with environment friendly and safe hydrocarbon membranes, a new versatile humidity generator was recently achieved, calibrated and implemented in the suite of dedicated ancillaries at KWS-2. These innovations will enhance the performance of the instrument by overcoming the current lack of specialized ancillary equipment and capabilities for the thorough structural characterization of systems of interest for applications in energy, health and smart materials. They will be available for the user program at KWS-2 when the MLZ FRM II reactor is put back into operation, as planned for the end of 2025.

## 2. Instrument description – current performance

KWS-2 is supplied with neutrons via a neutron guide that has been optimized to transport high neutron intensities to the sample position. A maximum neutron flux of $2 \times 10^8$ n $cm^{-2}$ $s^{-1}$ is available on the sample for $\lambda = 4.5$ Å with $\Delta\lambda/\lambda = 20\%$ when the shortest collimation length of $L_C = 2$ m is used (Radulescu 2012a; Houston 2018). In combination with the fast readout electronics of the $^3$He tubes main detector with count rates in the MHz range, this enables the measurement of high-quality scattering data from weak scattering samples such as diluted solutions of small proteins (Fig. 1).

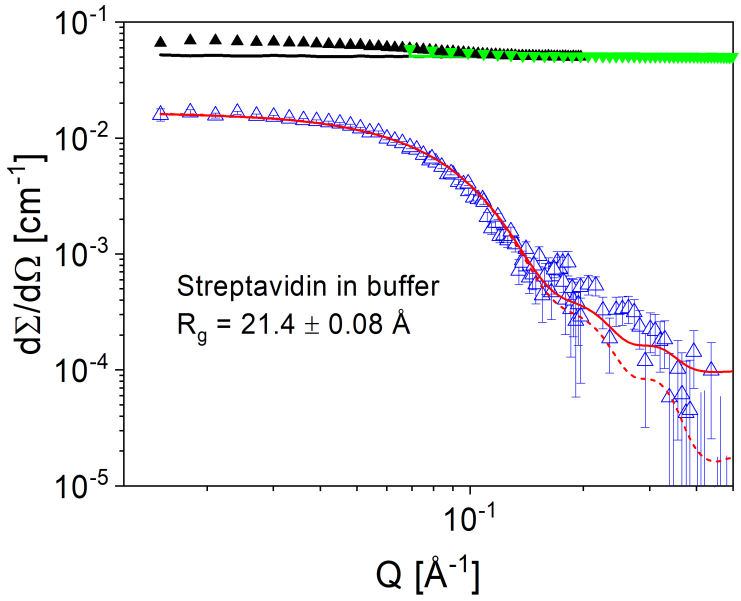


**Figure 1** SANS pattern of streptavidin protein (0.5 mg/ml) in buffer solution (Houston et al., 2018). The green and black solid symbols and the lines represent the experimental scattering patterns of the protein solution and buffer, respectively, recorded at detection distances of $L_D$ = 4 m (black) and $L_D$ = 1.5 m (green) with $\lambda$ = 5 Å over an acquisition time of 1800 s in each configuration. The open blue symbols show the protein scattering pattern after correction of the buffer contribution. The red curves show the calculated scattering pattern based on the respective PDB structure (PDB code 1n7y) using the computational code PEPSI-SANS, ILL Grenoble (Grudinin et al., 2017): with (solid) and without (dotted) consideration of the incoherent background.

On the other hand, the versatile velocity selector (Airbus, Germany) enables an easy selection of the wavelength $\lambda$ and wavelength spread $\Delta\lambda/\lambda$, depending on whether the specific scientific experiment demands either an improved resolution, thus $\Delta\lambda/\lambda$ = 10%, or a high intensity, hence $\Delta\lambda/\lambda$ = 20%, by operating it in either the standard configuration, parallel to the beam-axis, or in a tilted position with $\xi_i = -10°$ with respect to the beam-axis. The resolution can be further improved down to $\Delta\lambda/\lambda$ = 2%, in a range where no velocity selector can compete (Radulescu et al., 2015a; Radulescu, 2024), by using the TOF mode with the versatile double disc chopper providing a variable slit opening and a variable frequency, to match the optimal TOF conditions depending on the wavelength $\lambda$ and the sample-to-detector $L_D$ used. An example of the instrumental resolution at KWS-2 as tunable in a quick user-friendly manner from the instrument control script is shown in Fig. 2: the scattering features of the measured spherical form factor of $SiO_2$ size-standard spheres with low polydispersiy in

size (R = 242 Å, σ = 0.035) are revealed in more details with improvement of the Δλ/λ between 20% and 5%.

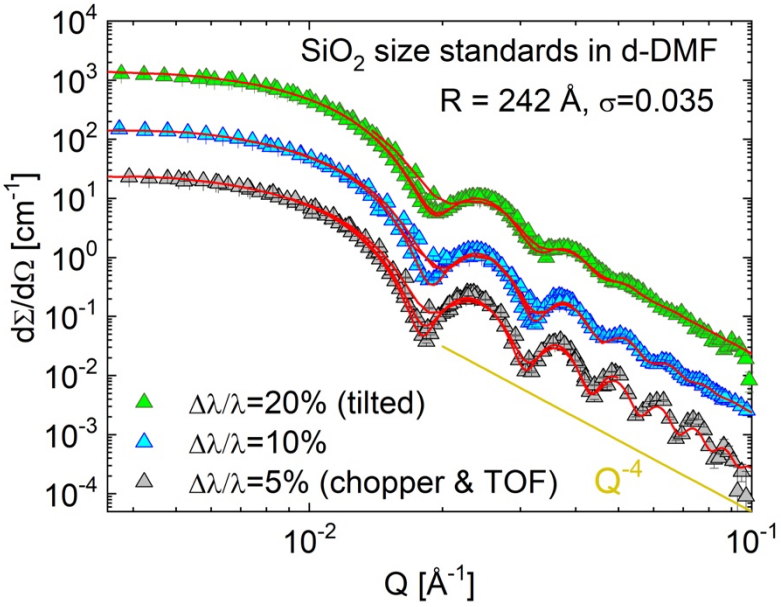


**Figure 2** SANS pattern of spherical $SiO_2$ particles with low polydispersity σ in deuterated dimethylformamide (d-DMF). The experimental data (symbols) were measured at different resolutions as defined by tuning Δλ/λ with the velocity selector in parallel or tilted orientation to the beam axis or the velocity selector-chopper tandem at KWS-2. The red curves represent the fit according to Eq. 9 in Radulescu et al. (2015a)

High resolution SANS using the TOF mode at KWS-2 is helping in the characterization of long range ordered systems such as micellar lattices (Amman et al., 2015), of interest in gel type pharmaceutical formulations (Puig-Rigall et al, 2020; 2021). Tilting of the velocity selector with respect to the beam axis shifts the $\lambda_{min}$ available at the instrument from 4.5 Å in the standard configuration to 2.8 Å, that enables a $Q_{max}$ = 1.0 $Å^{-1}$ to be currently reached. This is beneficial for the study of small morphologies such nanoscale water clusters in various matrixes (Schiavone et al., 2023; Pabst et al., 2021). For proteins in solution this is particularly interesting because a detailed analysis can be carried out in terms of structural models while considering their coherent and incoherent scattering contributions after corrections for the instrumental and buffer contributions were applied. Figs. 3-4 show the scattering from the alcohol dehydrogenase (ADH) protein (Sigma-Aldrich) in buffer solution at different protein concentrations, 5, 10 and 20 mg / ml (Fig. 3) and the protein scattering

after the correction for the buffer contribution was applied, together with the coherent and total scattering contributions, as calculated based on the atomic PDB structure (4w6z) up to Q = 1.0 Å$^{-1}$ (Fig. 4).

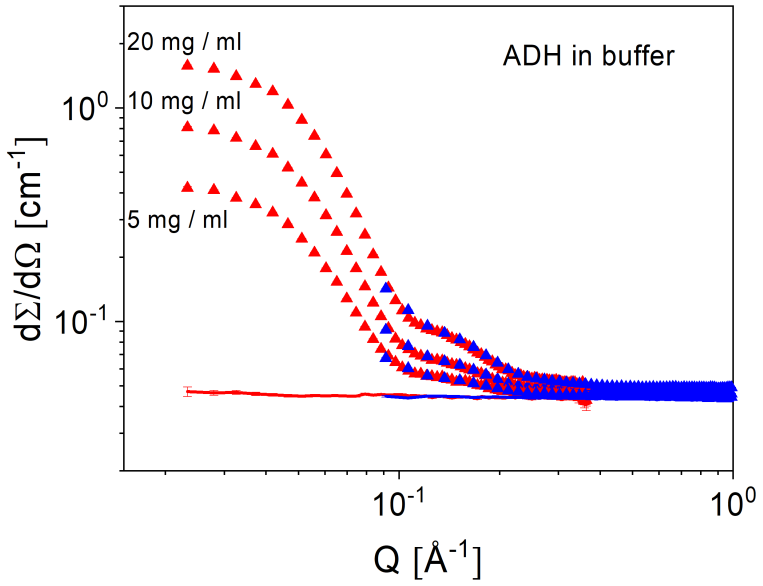


**Figure 3** Measured SANS patterns of ADH protein at different concentrations in buffer solution. The symbols indicate the results from the protein solutions, while the lines show the contribution of the buffer solution to the scattering. Results collected at $L_D$ = 4 m and 1.5 m are shown in red and blue, respectively.

After scaling by concentration the buffer corrected data fall on top of each other except at low Q where a small influence of the structure factor was observed in case of the higher concentrations. For modelling of the form factor the lowest concentration for the low Q region, to reduce structure factor effects, and the largest concentration for high Q because of the improved statistics were considered.

For the form factor calculation based on the respective PDB structures the computational code Jscatter (Biehl, 2019) was used. The data were smeared according to Pedersen et al. (1990) taking into account the wavelength spread $\Delta\lambda/\lambda$ = 14% (Radulescu, 2024) and the geometry of the instrument for the two selected detector distances. A good aggrement between the PDB structure and measured data was found with regard to main scattering features (Fig. 4): the Guinier regime at low Q, the characteristic two shoulders at 0.15 Å$^{-1}$ and 0.28 Å$^{-1}$, and the plateau at higher Q that is strongly dominated by the incoherent

contribution. The code calculates the incoherent scattering based on all atoms present in the atomic structure including incoherent contribution from a larger density in the hydration layer.

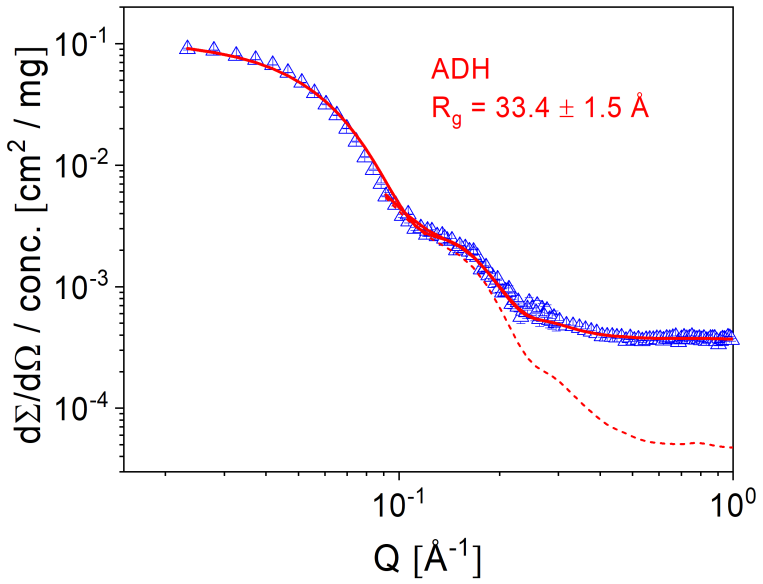


**Figure 4** SANS pattern of the ADH protein after correction for the buffer contribution (open symbols) and the scattering patterns calculated with the calculation code JScatter (Biehl, 2019): with (solid) and without (dotted) consideration of the incoherent background.

Finally, a $Q_{min}$ = 2 x $10^{-4}$ Å$^{-1}$ is enabled by the focusing mode at KWS-2, in which the parabolic $MgF_2$ lenses placed 1.5 m in front of the sample are used at 70 K to improve transmission by suppressing the scattering of phonons in the lens material, combined with a small entrance aperture (2 mm x 2 mm) at $L_C$ = 20 m and a high-resolution scintillation detector (HRD) at $L_D$ = 17 m, with a position resolution of 1 mm. The HRD is parked in a tower of the detector tank (Radulescu et al., 2012a) and can be brought into the beam on demand when the main SANS detector is parked at 20 m. The thorough characterization of polymer gels (Kaneko et al., 2024; Talley et al., 2019) or of complex assemblies of proteins with polymers or lipids (Krugmann et al., 2020) over a wide size range benefits from the advantages of combined focusing and pinhole modes on the same instrument for the structural investigation of samples that have undergone very specific thermal or compositional preparation, which would have required a high degree of reproducibility if an additional beamline had been included in the investigation to cover a wide Q range.

## 3. New upgrades

### 3.1. In-beam SEC complementarity

For the systems that dynamically form into oligomer states or systems that are prone to form aggregates, the collected small-angle scattering (SAS) data contain scattering from both the aggregates and the individual molecules. For such systems, an in situ fractionation method is necessary before the SAS measurement, in order to separately collect scattering data of different species. Size exclusion chromatography (SEC) is a technique to fractionate particles by different sizes in a mixture. SEC instrument is typically equipped with a pump which provides a steady flowrate of the elute buffer, bringing the injected sample solution to go through the elution column. The column is stuffed by gel particles with voids having specified sizes. During the elution of the sample, large particles are flushed out of the column at an early flushing time because they are excluded from going into the small voids. On the other hand, small particles are flushed out of the column at a late flushing time due to the relatively long traveling path, as they travel through the small voids in the column. Downstream of the column, a UV-vis detector records the flushing time of different-sized particles, which is used to examine the fractionation performance of the SEC instrument.

The in situ SEC option combined with SAS has been commonly achieved and continually upgraded at synchrotron X-ray facilities worldwide (Ryan *et al.*, 2018, Thureau *et al.*, 2021, Shih *et al.*, 2022), as well as several successful setups with in-house small-angle X-ray scattering (SAXS) machines (Bucciarelli *et al.*, 2018, Inoue *et al.*, 2019). The so-called SEC-SAXS technique has made large contribution to the biomedical field in the sense of its ability to resolve structures of individual bio-molecules. For small-angle neutron scattering (SANS), the first ever SEC-SANS setup worldwide was achieved at the D22 instrument at the Institut Laue-Langevin (ILL) (Jordan *et al.*, 2016, Martel *et al.*, 2023). Comparing to SEC-SAXS, the benefit of SEC-SANS is the opportunity to perform contrast matching and deuterium labeling for the targeted molecules, and is especially suitable to resolve structure of multi-component bio-molecules (Johansen *et al.*, 2018).

At KWS-2 a SEC instrument has now been established in-line with SANS, aiming to provide the SEC-SANS combination to its user community when the FRM II reactor will resume its activity. The flowchart design of the SEC-SANS instrumental setup is shown in Fig. 5. The chromatography is performed with the Knauer AZURA fast protein liquid chromatography

(FPLC) system, which is equipped with an auto-sampler, a binary pump as the elution pump, an isocratic pump as the rinse pump, a UV-vis detector, a refractive index (RI) detector, two conductivity detectors and a fraction collector. The setup is furthermore combined with a multi-angle light scattering (MALS) machine. The UV-vis detector, referred to as "1st UV" in the following content, is connected right downstream of the elution column, with a light path of 3 mm. The column used for all the following test measurements was Superdex200 10/300 (Cytiva, L × I.D. 30 cm × 10 mm), suitable for protein molar mass within the range of 10-600 kDa. Due to the limited space around the sample stage of KWS-2, the FPLC system, equipped with the "1st UV" detector, (Figure S1a) is located at an elevated platform above the experiment hutch (Figure S1b), with a distance of 2.5 meters up to the SANS sample cuvette. A switch valve (Fig. 5, red valve) is installed between the 1st UV and the SANS flow cuvette, which allows only the fractions of interest to flow into the SANS flow cell for neutron exposure and SANS data collection. This way, contamination of the cell by the unwanted fractions is avoided, and thus the SANS data of the interested molecules is not compromised.

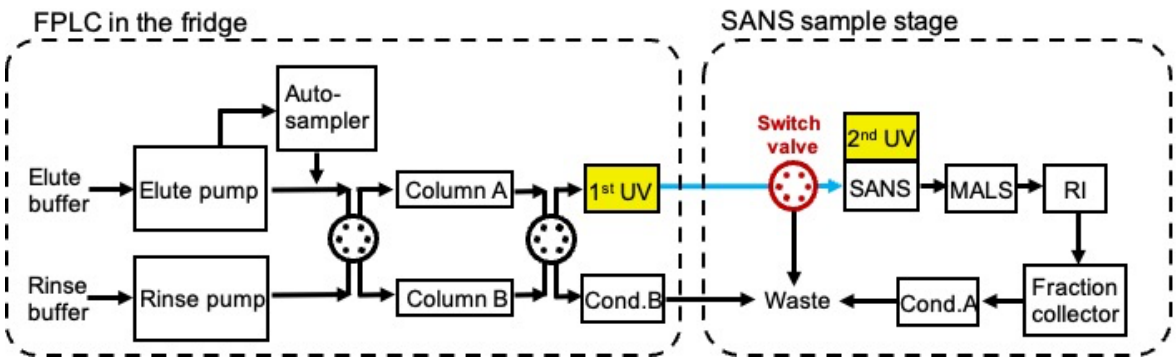


**Figure 5** SEC-SANS flowchart at KWS-2, showing the sample flow path and the key components. The yellowish blocks mark the two UV detectors at FPLC and at SANS stage, respectively. The blue line indicates the connecting capillary transferring the sample from the FPLC system to the SANS measurement. The switch valve upstream of SANS is marked in red.

The SANS cuvette holder is mounted at the sample stage (Figure S1c), where a second UV-vis spectrometer, the "2nd UV", is installed to monitor the samples flowing through the SANS sample cuvette. It consists of a light source (DH-2000-DUV lamp, 190-2500 nm, Ocean Optics), a spectrometer (FX UV-Vis, Ocean Optics) and optical fibers and collimating lenses (74-UV, Ocean Optics). The four-side polished SANS flow cuvette is placed inside a thermostated holder with Peltier elements, where the solution capillaries and the cuvette are

sealed together using epoxy resin AB glue. The design of the SEC complementarity at KWS-2 follows the boundary conditions imposed at the sample postion of the instrument and the main components and processes were optimized for providing the SANS instrument with the desired sample quality, also providing the users with information on the realistic initial conditions required by the sample purification process. An obvious drawback of the setup at KWS-2 compared to similar setups at other beam-lines is the large dead volume of the system. Dead volume is the total volume that the sample flows through in the system, and it is strongly related to the separation performance of FPLC. When the sample solution is injected into the FPLC instrument and flows in the capillary, it is concentrated, therefore a sharp UV absorbance peak is detected by the "1st UV". After flowing through a long distance in the SANS cuvette, it becomes diluted by the continuous flow with the elute buffer, resulting in a broadening of the elution peak. Namely, the longer traveling distance for the injected sample, i.e., the larger dead volume, the more diluted the sample, and more serious the peak broadening effect. Thus, to improve the separation efficiency of FPLC instruments, the dead volume of the system was minimized following detailed test measurements. Also, the fractionation performance of FPLC system is often evaluated by the dilution factor of the injected sample solution, i.e., the original concentration divided by the concentration after elution.

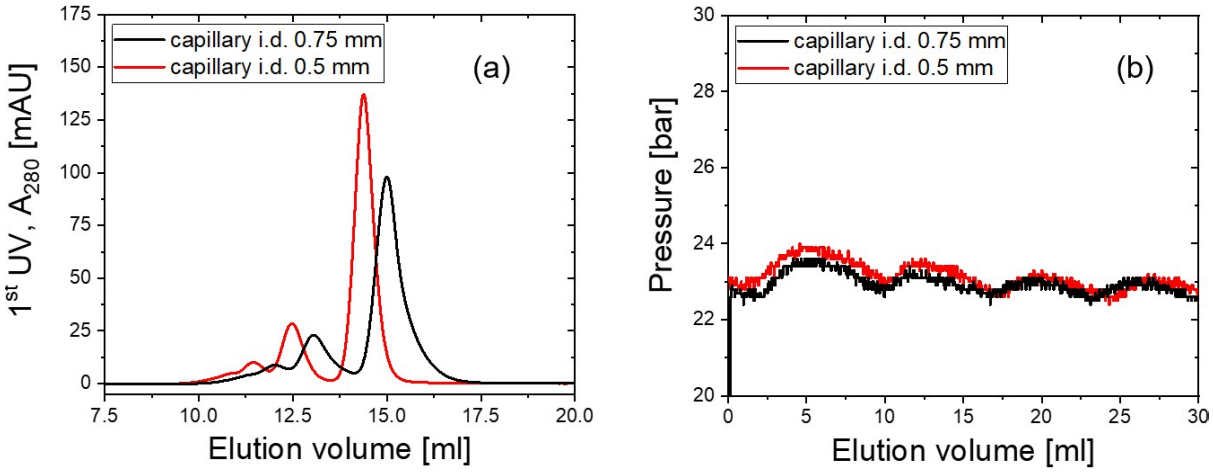


**Figure 6** (a) Elution profiles of 10 mg/ml BSA solution with capillary i.d. = 0.75 mm (black curve) and i.d. = 0.5 mm (red curve). (b) The corresponding pump back pressure during the measurement

The FPLC system at KWS-2 was brought to functioning, with its solution capillary having inner diameter (i.d.) of 0.75 mm. A testing measurement on its fractionation efficiency was performed with a 10 mg/ml bovine serum albumin (BSA) solution, and an injection volume

of 200 µl, eluted by phosphate buffered saline (PBS). The elution profile (Fig. 6a, black curve), expressed by plotting UV absorbance at 280 nm, $A_{280}$, along elution volume, shows signal of large aggregates, and peaks of BSA trimer, dimer and monomer, subsequently from low to high elution volume. The asymmetric monomer peak and the poor separation between peaks are supposed to be the peak broadening effect due to the large dead volume of the system. The monomer concentration at its peak position is thus calculated to be 1.52 mg/ml.

A better chromatography performance, a smaller dead volume of the system was achieved by replacing the capillaries by the ones having i.d. of 0.5 mm. The elution profiles after changing the capillaries (Fig. 6a, red curve) shows symmetric elution peaks and improved peak separation. The monomer peak gives a concentration of 2.12 mg/ml, i.e., a 40 % of concentration increase compared before the capillary replacement. In the meantime, reducing capillary i.d. comes with the risk of an increase of the pump back pressure (Cytiva, 2020), which might put the column in danger. The back pressure change before and after replacement of the capillaries was inspected and it was observed that the back pressure, measured at the elution pump, with i.d. = 0.5 mm (Fig. 6b, red curve) is slightly larger than the one with i.d. = 0.75 mm (Fig. 6b, black curve), but it stays still far under the bearing limit of the column, i.e., 50 bar. Considering the dilution factor of the BSA monomer, the monomer concentration in the sample is obtained from the integration fraction of the monomer contribution in the elution profile. For the measurement with capillary i.d. = 0.75 mm, the monomer concentration in the injected sample solution is 7.35 mg/ml. Providing the monomer concentration after elution to be 1.52 mg/ml, the dilution factor was calculated to be 4.84. For the measurement with capillary i.d. = 0.5 mm, the monomer concentration in the injected sample solution is 7.37 mg/ml, and the monomer concentration after elution is increased to 2.12 mg/ml. The change leads to a reduced dilution factor to be 3.48.

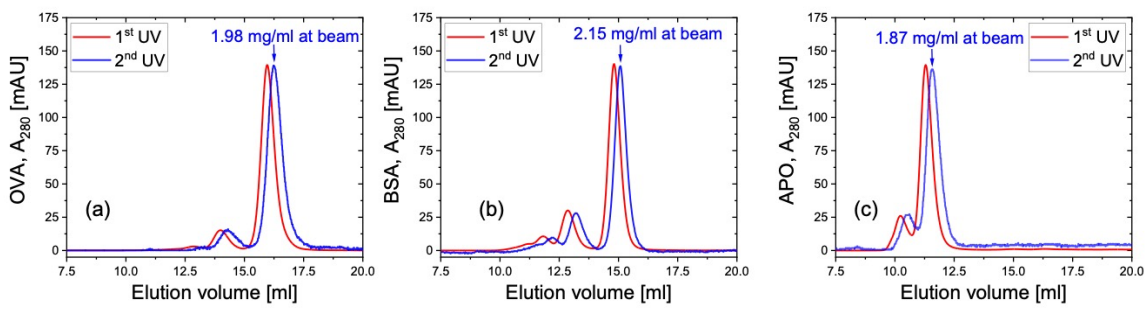

**Figure 7** Elution profiles of 10 mg/ml (a) chicken ovalbumin, OVA, (b) bovine serum albumin, BSA, and (c) apoferritin, APO. The maximum monomer concentration from the 2nd UV profile is written above the corresponding elution peak. All $A_{280}$ are normalized by light path.

The monitoring of the arrival of the fractioned sample from the FPLC system to the SANS sample cuvette is achieved with the "2nd UV" that provides an in situ information about the sample in the flow cuvette during the SEC-SANS measurement. Considering the spatially separated FPLC instrument and the SANS stage, it is important to check how much the UV signal changes from the 1st to the 2nd UV after the sample flows through the of 2.5-meter capillary (i.d. = 0.25 mm).

Measurements of the elution profiles were carried out on different protein solutions with the 2nd UV aiming at the front face of the SANS flow cuvette to learn about the protein concentration for SANS data collection. A customized flow cuvette with a light path of 1 mm for the neutron beam and a small inner volume of around 135 µl is used for the SEC-SANS measurements (Fig. S1c). Three proteins with different molar mass are chosen for the examination measurements: chicken ovalbumin, OVA (45 kDa), bovine serum albumin, BSA (66 kDa) and apoferritin, APO (454 kDa). Their elution profiles of the 10 mg/ml solutions from the 1st UV and the 2nd UV are shown in Fig. 7a,b,c, respectively. The UV absorbance at 280 nm, $A_{280}$, is normalized by light path of the two devices for comparison. It can be noticed that, for all the three samples, there is only small changes between the 1st UV and the 2nd UV. Namely, despite the long capillary between the FPLC instrument and the SANS sample stage, the separation resolution of the chromatography does not become worse throughout the flowing. For each sample, maximum $A_{280}$ of the monomer peak from the 2nd UV profile is used to calculate the monomer concentration, so that the protein concentration at the neutron beam can be estimated from:

$$A_{280} = \varepsilon_{280} c l \qquad (1)$$

where $c$ is the concentration, $l$ the light path and the extinction coefficients at 280 nm $\varepsilon_{280}$ for 0.1 % solution and 10 mm light path, are $\varepsilon_{0.1\%,\,OVA} = 0.701$ (Pace *et al.*, 1995), $\varepsilon_{0.1\%,\,BSA} = 0.646$ and $\varepsilon_{0.1\%,\,APO} = 0.729$ (Graewert *et al.*, 2020) for the three proteins respectively. The calculation gives 1.98 mg/ml for OVA monomer peak, 2.15 mg/ml for BSA monomer peak and 1.87 mg/ml for APO monomer peak. Dividing the monomer concentration in the original sample by the monomer concentration obtained at 2nd UV, the dilution factor for OVA, BSA

and APO is found to be 4.37, 3.40 and 4.53, respectively, which are comparable values with the other SEC-SAS instruments. The small UV absorbance variation from the 1st UV to the 2nd UV is attributed to the thin inner diameter (0.25 mm) of the connecting capillary as well as the small inner volume of the flow cell, which together help in suppressing the dilution effect. The presented experimental results provide information on the sample condition for SEC-SANS measurements at KWS-2: with injected protein concentration of 10 mg/ml and volume of 200 µl, the obtained concentration in the center of the flow cell for neutron exposure will be around 2 mg/ml, and a dilution factor around 4, while one should also note that the actual experimental results may vary depending on the individual samples.

During practical SEC-SANS measurements for commissioning, the 2nd UV will be installed in the way that the light penetrates the flow cell on the direction perpendicular to the neutron beam (schematically demonstrated in Fig. 8a). This means, it goes through the side window of the cell, where the light path is 9 mm. To inspect the feasibility of such configuration, the experiments mentioned above were repeated, with the UV light shedding on the side window of the flow cell. Data collected by the 2nd UV at the side window (Fig. 8b, dash-dotted orange curve) is plotted together with that collected at the center of the front window (Fig. 8b, solid blue curve), and $A_{280}$ is normalized by the light path. The distinct elution peaks collected at the side of the flow cell align well with those collected at the front window, suggesting that the signal collected from the 2nd UV serves as good indicator for an in-situ monitoring with simultaneous SANS measurements. It is noticed that $A_{280}$ of the elution peaks is smaller when data is collected at the side of the flow cell, especially for monomers, indicating a dilution effect along the horizontal direction during elution. UV signal at different positions along the vertical direction were also detected (i.e., along the sample flowing direction), showing rather small dilution effect (Fig. S2). Considering the typically applied neutron beam of 4x6 $mm^2$ at KWS-2, with a shorter size along the horizonal direction, the aim to obtain single particle scattering of the targeted protein should be achievable. However, the feasibility measurement will be carried out with neutrons, and the SANS data obtained in this way will be analyzed thereafter.

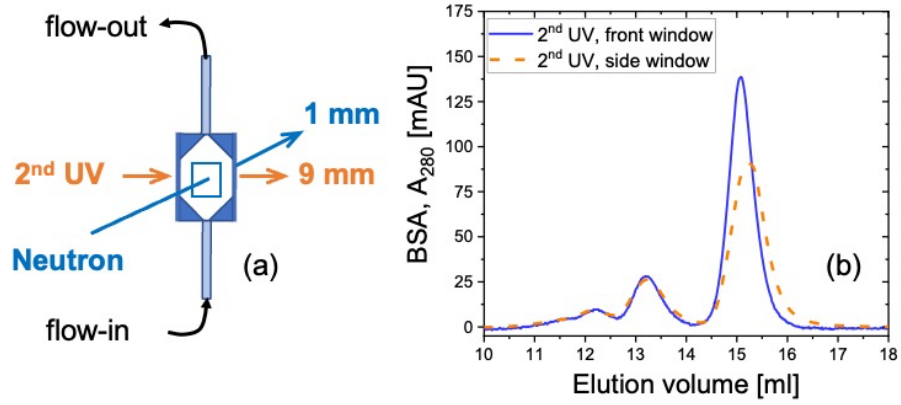


**Figure 8** (a) Schematic demonstration on the manner how neutron beam and the 2nd UV light penetrate through the flow cell during practical SEC-SANS measurements. The corresponding light path is written aside. (b) Elution profiles of 10 mg/ml BSA solutions collected from the 2nd UV when light penetrates the SANS flow cell on the side window (dash-dotted orange curve) and on the front window (solid blue curve) are plotted for comparison. All $A_{280}$ are normalized by light path.

In cases when only the selective specie after the elution is to be measured by neutron, while the rest of the species are not of interests, a switch valve installed right upstream of the SANS flow cell serves to control the flow path in the manner that only the interested elution peak flows into the cell for SANS data collection, while the rest of the elution peaks are directed to the waste (see Fig. 5 for the flowchart). Elution measurements on 10 mg/ml BSA solution were performed to demonstrate the concept, where the switching function was programmed in the FPLC controlling software. During the so-called "flow through" measurement, where the switch valve was not utilized and all the species after chromatography go into the flow cell, the elution profile from the 2nd UV shows signal from aggregates, trimers, dimers and monomers (Fig 9, solid blue curve). In another measurement where the switch valve was utilized, the valve position shifts accordingly to the elution volume (EV). Between 0 – 8.5 EV, the solution flows into the SANS flow cell, so that SANS data of the buffer flowing through the cell can be collected to facilitate the SANS data reduction. Then, between 8.5 – 14.0 EV, the flow was guided to the waste, as the structural information of the aggregates, trimer and dimers are not of interest in the current case. Finally, between 14.0 - 25 EV, the valve shifts again to send the monomers into the cell for SANS data collection. Thus, the obtained elution profile from the 2nd UV shows a single peak attributed to the monomers (Fig.

9, dash-dotted green curve). The fact that the two elution profiles overlap nicely in EV range of the monomer peak indicates that the influence on the sample from the additional valve on the flow path is small and negligible.

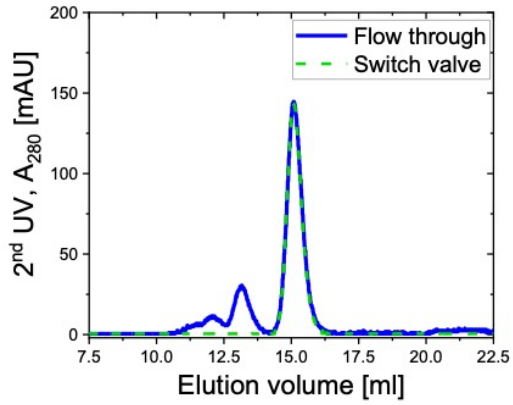


**Figure 9** Elution profiles of 10 mg/ml BSA utilizing the switch valve (dash-dotted green curve) and not utilizing it (solid blue curve). $A_{280}$ is collected from the 2nd UV at the front window of the flow cell.

At KWS-2, with a maximum flux of $2 \times 10^8$ n cm$^{-1}$ s$^{-1}$ at the sample position combined with the rapid readout detection electronics capable to work in list mode, the buffer-subtracted scattering curve of protein solution as dilute as 0.5 mg/ml (Fig. 1) shows pretty well defined scattering features. Based on this result, the SEC-SANS setup at KWS-2 shall enable clear scattering curves for samples with a concentration above 1.2-1.5 mg/ml after chromatography when the user program at MLZ will be resumed. Still, the data quality depends on several factors of the sample, e.g., scattering contrast and molar mass. A thorough discussion including MALS and RI analysis will be reported elsewehere.

### 3.2. In-beam RH & T variation on the sample

The characterization of polymeric films and membranes under controlled humidity conditions has received significant attention especially in energy relevant studies (Bose et al., 2011; Grzybek et al., 2024; Song et al., 2022; Adamski et al., 2021; Luo et al., 2020).

Proton- and anion-exchange polymeric membranes produced by various methods to target improvement in either the conductivity in various T and RH conditions or the durability after exposure to the application conditions were intensively studied at KWS-2 so far (Zhao et al.,

2021; 2022; Yoshimura et al., 2024). However, most of the studies were focused on membranes in saturated state (equilibrated) in $H_2O$, $D_2O$ or mixtures, to apply the contrast variation and get a much clearer view of the structure and morphology of the polymer material and water domains in this condition. Less studies dealt with the in-beam variation of RH and T on the sample due to the lack of a robust, competititve and versatile sample environment that should have provided the full control of the variation of RH, T and contrast (type of hydration water) on the sample in-beam, over a long time, and incorporated in the control software of the instrument. With the advent of intensive studies for finding a non-hazardous and environmentally friendly alternative to the perflourinated Nafion, the need for such a neutron scattering dedicated sample environment for serving microstructural and microdynamical characterization of various materials increased.

From the experience collected at J-PARC, where a $D_2O/H_2O$ vapor generator for contrast variation neutron scattering was achieved and implemented with appropriate sample chambers in the user program at different instruments, such as SANS, reflectivity and quasi-elastic neutron scattering (QENS), we came to the idea of incorporating a similar humidity generator in the user program at KWS-2 for applications on hydrated polymer or biological membranes. The central piece of the setup is a precise dewpoint generator which was customized for neutron scattering purposes by the company microEquipment (Tokyo, Japan), which will be used in the near future at KWS-2, when the user program at the FRM II reactor will be resumed, coupled to a multiposition sample chamber that is thermostated itself for providing the needed temperature on the samples in beam and requesting the appropriate dew point conditions at the generator for obtaining the desired RH on the sample (Figure S3a). The experimental setup for SANS studies under controlled RH/T/contrast conditions is described in details by Arima-Osonoi et al. (2023) with regard to the working principle, calibration and efficiency on some selected scientific cases. We have used successfully the same setup for the thorough structural characterization by SANS of functionalized (proton conductive) syndiotactic-polystyrene membranes under various RH/T/contrast conditions (Schiavone et al., 2023). The precise dewpoint generator incorporates two identical vapor-generation systems, each capable of independently producing $D_2O$ and $H_2O$ vapor and comprises four gas lines with mass flow controllers (MFCs) and valves, two saturators, and a PID (proportional–integral–derivative) controller to regulate the gas flow rate and temperature. Vapors with dew points ranging from +5 to +85 °C are generated and two

distinct techniques – the two-temperature and divided-flow methods – are applied to obtain the required RH on the sample (Arima-Osonoi et al. 2023).

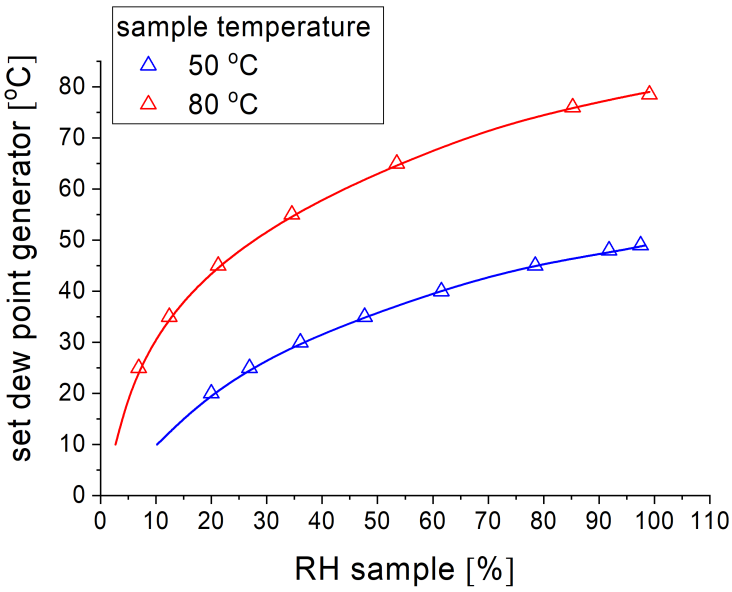


**Figure 10** Selected calibration curves of the humidity generator for the sample chamber at different temperatures: the dew point set at the generator vs. measured RH in the sample chamber with the dew point mirror sensor for $H_2O$ vapors – symbols and $D_2O$ vapors – lines.

The generated humidity is transported to the neutron scattering instrument via a 4 m long supply line, which consists of flexible stainless steel pipes with a diameter of 3/8 inch and is insulated with an Aeroflex plate. All moisture gas lines are equipped with silicone rubber heaters that can heat up to 100 °C. As in the case of the SEC complement, this long tube overcomes the space limitations at the KWS-2 beamline sample position that prevent placement of the generator near the sample chamber within the shielded hutch at the KWS-2 sample position. Several components, including the PID controller and valves, are controlled and monitored by a programmable logic controller (PLC) that interfaces with the KWS-2 instrument control system. This integration facilitates remote data acquisition and the automated running of experiments. According to the experience obtained at J-PARC, the generator features, the storage tanks and the automatic water pumps will allow several days of continuous operation without manual water supply.

For KWS-2, a multi-position thermostated sample chamber was designed to be used in combination with the humidity generator (Fig. S3b), allowing the measurement of multiple samples at controlled RH and T conditions. The chamber is equipped with thin Al windows

(0.5 mm) and water-circulating internal channels to allow precise temperature control with ± 0.5 °C between RT and 85 °C via a Julabo water bath. The system was calibrated with a high-precision Michell S8000 chilled mirror hygrometer (PST GmbH, Friedrichsdorf, Germany) to determine the dew point that must be set on the generator to obtain the desired RH on the sample as a function of sample temperature (Fig. 10). No observable difference in calibration curves for the $H_2O$ and $D_2O$ was obtained. The information from the mirror hygrometer is stored in the recorded data file after the SANS measurement together with the information set on the generator and the sample temperature. Since a detailed characterization of a similar humidity generator performed at J-PARC has already been reported elsewhere (Arima-Osonoi et al, 2023), we report here the results of a specific experiment to demonstrate the efficiency of the newly achieved humidity generator at KWS-2, which involved measuring the conductivity of Nafion117 membranes at different RH and T conditions using a BT-115 4-electrode cell from Electrochem Inc. coupled to the humidity generator (Fig. S4) and comparing it with known literature data. A Hioki IM3523 LCR meter (Ueda, Japan) was used to interpret the data from the conductivity cell, while a TC-3000 controller from AS ONE (Osaka, Japan) was used to control the temperature on the conductivity cell. The choice of Nafion117 was due to the known proton conductivity of this type of membrane at various RH and T conditions, which enables us to assess the performance of the humidity generator at optimal measurement conditions.

Fig. 11 shows the measured proton conductivity at different RH and T values of a Nafion117 membrane, as received (Chemours, Wilmington, DE, USA), parallel to that of a uniaxially deformed Nafion117 membrane (in-plane along the deformation axis). The deformed membrane was prepared with a deformation ratio of 2.0 compared to the initial length using a Linkam Modular Force Stage (Linkam Scientific Instruments, Salfords, UK). Both data sets are compared with literature data on the same systems as reported by Wang et al. (2002) for the Nafion117 membranes and by Park et al. (2011) and Klein et al. (2013) for the stretched Nafion117 membranes.

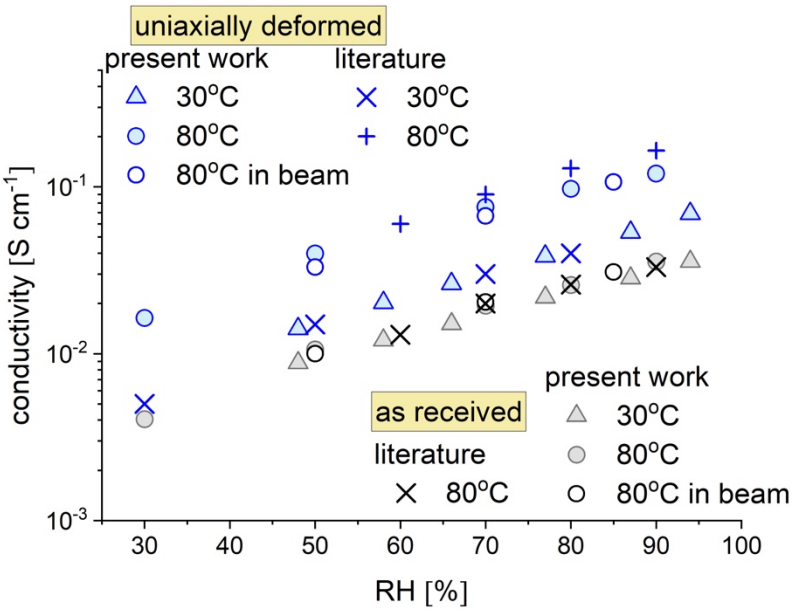


**Figure 11** Evolution of the ionic conductivity measured on Nafion117 membranes as received (black symbols) and uni-axially deformed (blue symbols), as a function of the RH on the sample (obtained with $H_2O$ vapors): data measured at 30 °C (triangles) and 80 °C (circles). The data at 80 °C were collected either as part of laboratory measurements at JCNS (full symbols) or in the neutron beam (empty symbols), simultaneously with SANS, at J-PARC. The × and + symbols represent literature data (same color code): black × Wang et al. (2002); blue × Klein et al. (2013); blue + Park et al. (2011). The conductivity measured in-plane along the deformation axis is displayed for the uniaxially deformed membranes.

There is good agreement between our data and the literature data in terms of both the quantitative values and the qualitative RH and T behavior. Our data confirm the known behavior of Nafion117 membranes, which show increasing conductivity values with increasing relative humidity and only a very small difference between the conductivity values at 30 °C and 80 °C, as reported by Sone et al. (1996). Furthermore, the striking difference between the conductivity values at 30 °C and those measured at 80 °C in-plane along the deformation axis on stretched Nafion117 membranes indicates that our data are consistent with those of Park et al. (2011) and Klein et al. (2013). The much higher values observed at 80 °C, which increase with increasing relative humidity, must be related to structural features of such deformed membranes, where the water accumulated at high temperature apparently organizes in oriented domains, a morphology that facilitates the development of consistent and continuous conductive paths along the deformation direction of the membrane, as reported by Allahyarov & Taylor (2009). The good performance of the newly achieved

humidity generator for KWS-2 was further confirmed by the conductivity measurement on the same Nafion117 membranes using the similar humidity generator at the J-PARC and the in-beam conductivity cell with a Hioki 3532-80 chemical impedance analyzer at the BL-15 Taikan SANS-WANS beamline (empty circles in Fig. 11; for the cell setup see Fig. S5). Although the simultaneous SANS and conductivity measurement data from these Nafion samples, including the contrast variations applied to the hydrated domains, will be the subject of a forthcoming manuscript, Fig. S6 shows a selected set of SANS data to demonstrate the strength of the experimental approach we have used. The scattering patterns from the as-prepared sample and the uniaxially deformed sample are similar to those reported by Rubatat & Diat (2007). The four main scattering features of Nafion membranes for the as-received film sample can be clearly identified from the experimental data: at low Q - the power law characteristic of the large-scale fractal morphology of the membrane (1); at medium Q - the matrix knee characteristic of the SLD variation between crystalline and amorphous domains in the material (2); at higher Q - the ionomer peak indicating the correlation between the ion clusters in the hydrated domains of the membrane (3), and at very high Q - the first crystalline peak due to interchain correlations in the crystalline matrix of the material (4). After uniaxial deformation of the membrane, the intensity of the ionomer peak increases along the direction perpendicular to the deformation axis, an effect also observed by Rubatat & Diat (2007) and explained by the alignment of the scattering objects along the deformation axis and the formation of parallel arrangements. Moreover, the first crystalline peak is prominent on the axis perpendicular to the deformation direction, which has also been observed by Mendil-Jakani et al. (2015). This is related to the orientation of the crystalline lamellae along the deformation direction, such that the main crystalline planes are oriented perpendicular to the deformation direction.

### 3.1. WANS

Materials based on semi-crystalline polymers exhibit a phase separation into crystalline and amorphous regions. These materials are characterized by a complex morphology with multiple hierarchically organized structural levels that span a wide length scale between several Å and hundreds of nanometres (Akpalu, 2010; Radulescu et al., 2015b; Kanaya et al., 2007). Moreover, the bulk and interlamellar amorphous regions can be functionalized, which results in even more complex morphologies when external stimuli such as humidity, temperature or elongation/compression are applied to the sample (Schiavone et al., 2023). For

the characterization of such complex morphologies, a wide length scale has to be covered, which usually requires a combination of different experimental methods in the structural analysis. Simultaneous use of wide- and small-angle scattering methods in the same experiment is necessary for sensitive or expensive samples, if special attention must be paid to sample preparation (composition, quality, amount etc.) or in-situ treatment (temperature, humidity, chemical condition etc.) during the experimental investigation (Tashiro & Sasaki, 2003). While modern X-ray laboratory diffractometers or beamlines at large-scale facilities can easily and successfully combine ultra-small-angle X-ray scattering (USAXS), small-angle X-ray scattering (SAXS) and wide-angle X-ray scattering (WAXS) (Pauw et al., 2021), in the case of neutron scattering such a combination of methods requires special care. WANS and SANS can be simultaneously performed without technical or organizational difficulties with time-of-flight (TOF) SANS instruments at spallation or steady state (reactor) neutron sources. In this case, a broad wavelength band is used and a wide angular range of scattering can be covered by using a large number of detectors, either movable (Heenan et al., 2005; Zhao et al., 2010; Sokolova et al., 2019; Dewhurst et al., 2016) or placed in fixed positions (Takata et al., 2014; Koizumi et al., 2020; Allen, 2023). On the other hand, equiping a classical pinhole SANS instrument at a research reactor with wide-angle detectors enables to extend the Q range towards higher Q values (Heller et al., 2018) and to access the diffraction mode, thus the possibility of bridging the atomic and meso-scales at the same instrument, provided that the instrument resolution can be tuned to serve the scientific goal.

A new detector consisting of $^3$He tubes array is currently being tested at JCNS with the aim of installing it for the WANS option at KWS-2. For this purpose, the first 1.7 m long cylindrical segment of the evacuated tank at KWS-2 is currently being replaced by a conical nose (Fig. S7), which will share the common vacuum with the rest of the tank. This geometry allows the WANS detector to be installed in a fixed inclined position above the transmitted beam axis at a distance $L_D$ = 1.25 m after the sample (Fig. 12). The neutrons scattered by the sample can be detected over a wide angular range simultaneously with the SANS detector (up to $\theta_s$ = 17.5°) and with the WANS detector (up to $\theta_s$ = 53°), both in continuous and TOF mode. In this detection geometry, a maximum value in the Q range of $Q_{max}$ = 2.0 Å$^{-1}$ is achieved, while working with neutrons of a wavelength $\lambda$ = 2.8 Å. A suitable $\Delta Q/Q$ resolution achieved with the resolution chopper (Radulescu et al., 2015a) and TOF data acquisition will allow detailed observation of crystalline peaks of semi-crystalline polymer systems, as shown in the recently published proof of principle (Radulescu, 2024). It is

expected that with this upgrade, measurements of similar quality to that of data collected at the BL-15 Taikan of the J-PARC (Schiavone et al., 2023) will also be possible at KWS-2.

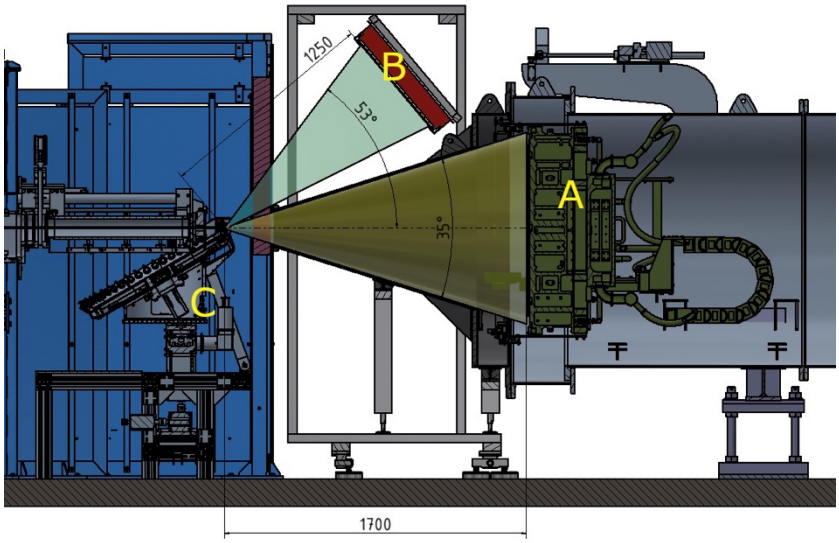


**Figure 12** Schematic representation of the SANS and WANS concept at KWS-2: the SANS angular range is shown in dark yellow (maximum $\theta_s$ = 17.5°), while the WANS angular range is depicted by the green field (maximum $\theta_s$ = 53°). The $L_D$ for the WANS detector and the minimum LD for the SANS detector are indicated in mm. The SANS detector at $L_D$ = 1.7 m is labeled A, the WANS detector at $L_D$ = 1.25 m is labeled B and the automatic sample changer (carousel with 48 positions) is shown at the sample position (C).

The WANS detector consists of an array of 80 $^3$He tubes and fast readout electronics supplied by Canon Electron Tubes & Devices (CETD, Otawara, Japan) and Clear Pulse (Tokyo, Japan). The $^3$He tubes with a diameter of 6 mm and an active length of 60 cm thus provide a detection field of approximately 50 cm x 60 cm for the WANS geometry. The tubes are filled with $^3$He and $CO_2$ as a stop gas, at a $^3$He partial pressure of 12 atm. According to the manufacturer, the detection efficiency is about 60 % for $\lambda$ = 3 Å and 80 % for $\lambda$ = 7 Å. The WANS detector will operate in air, which makes installation, maintenance and operation very simple. Based on the experience gained at J-PARC and JRR-3 at the SANS beamlines with the WANS detectors operated in air, a good WANS data quality is expected. However, the concept of the WANS option includes the installation of a helium or argon box in front of the detector to minimize the air path between the sample and the PSDs and to reduce the background and beam attenuation due to scattering on air. By using argon or helium at or

near ambient pressure, the pressure difference between the inside and outside of the box is negligible, so the box can be built with very thin windows. If it proves necessary during the commissioning tests, the helium or argon box can be installed to keep the background at a very low level. To mitigate the effect of the entrance window flange, which creates an angular gap between SANS and WANS detectors (Fig. 12), the Q overlap between WANS and SANS data can be adjusted by working with different wavelengths in the range of 2.8 - 5 Å and performing short measurements with both detectors in the high flux regime of the instrument, i.e. with the SANS detector at $L_D$ = 1.7 m. As previously reported (Radulescu, 2024), the instrumental resolution in the Q range between 1 and 2 $Å^{-1}$ depends practically only on $\Delta\lambda/\lambda$, with the collimation contribution having a negligible influence. This opens up the possibility of maximizing the intensity on the sample by using the shorter collimation length $L_C$ = 2 m, i.e. very short measurements, without compromising the quality of the data.

Fig. S8 shows the view of the detector as it consists of the ten 8-packs assembled into a 2D detection array. A second similar ensemble, to be installed symmetrically to the detector shown in Fig. 12 under the beam axis, may be considered for the near future. The DAQ middleware was developed at JCNS to communicate with the CETD firmware installed on the detector modules and to enable the correct data acquisition and sorting conditions to be set. Successful tests of a prototype of an 8-pack of $^3$He tubes were performed at JCNS and FRM II in 2023, motivating the purchase and installation of a full system at KWS-2. It should also be mentioned at this point that the $^3$He tube detectors supplied by CETD at the SANS-J instrument at the JRR-3 reactor in Japan (Noda et al., 2016; Kumada et al., 2023) and at the BL-15 Taikan at J-PARC (Takata et al., 2015) are successfully operating in both SANS and WANS measurement geometries, which has been a great support in the decision for choosing this type of detectors for the WANS option at KWS-2. The test of the prototype in 2023 and of the complete system in 2024 was performed with a $^{252}$Cf neutron source at the FRM II in Garching.

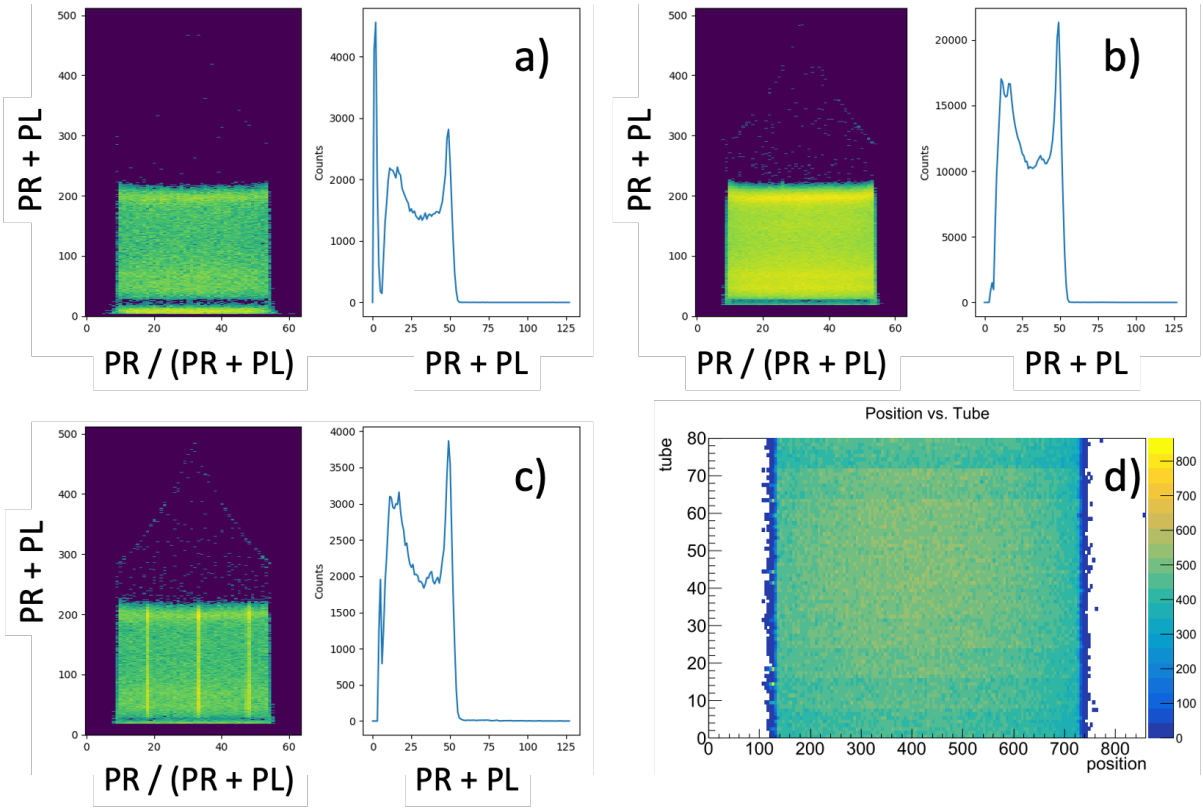


**Figure 13** Examples of position versus amplitude spectra (colored panels in a, b and c) and pulse height spectra (blue curves in a, b, c) measured with the detector during the test witht the $^{252}$Cf neutron source: (a) full spectrum; (b) the spectrum with the γ peak at lower channels (< 10) sorted out; (c) results with the absorbing mask with three narrow slits (3 mm) in front of the detector, with the slits transverse to the horizontal $^{3}$He tubes. In c), partial γ-peak discrimination was used during the middleware DAQ test. The flooding test of the entire detector with the $^{252}$Cf neutron source is shown in d). Position was obtained from the ratio of the right amplitude (PR) to the total pulse height (PR+PL).

The usual tests as described in our previous work on the optimization, installation and commissioning of the SANS main detector (Radulescu et al., 2016; Houston et al., 2018) were also performed with the CETD detectors. Fig. 13a-c show examples of the typical position/amplitude results and pulse height spectra collected in different seting conditions of the detector, as well as the image of detector flooding with the $^{252}$Cf neutron source (Fig. 13d). The typical pulse height distribution spectrum collected during the tests without γ discrimination is shown in Fig. 13a, right panel. The full energy peak can be easily observed just above channel no. 50, while the proton and triton peaks are yielded at lower channels. The narrow and intense γ-peak when not discriminated is observable at very low channels (<

10) while it is sorted out (Fig. 13b, right panel) when the γ discrimination through the JCNS middleware DAQ is applied. Full detector illumination data (Fig. 13d) were interpreted in terms of measured events across position and amplitude (energy) as exemplified in Fig. S9, which confirmed the good quality of the position-response of the detector. The position resolution was tackled on the prototyped module by using a Cd-mask with three slits carved across the 8-pack for a slit width of 3 mm (Fig. S10), while for the full detector a boron carbide mask with 3 slits of 2 mm width was used. Fig. 14 displays an example of Gaussian fit to peaks measured at two positions along a tube in ther full detector that yielded a position resolution of about FWHM ≈ 2.355 σ = 5.75 mm in the middle and towards the ends of the tube. However, this may be considered as overevaluated due to the compact measurement geometry with the detector placed too close to the $^{252}$Cf source. Thus the very wide divergence of beam falling onto the detector and the relatively large width of the slits used for the experiment leads to an overestimated position resolution. The precise position resolution detector along the $^{3}$He tubes remains to be confirmed again with neutrons at KWS-2 where the high intensity will enable the use of a much narrow slit opening (1 mm width). Following the lab tests, it can be considered that the newly achieved detector perfoms well. The installation at KWS-2 is currently in progress, with the goal of having the WANS option operational for the expected restart of the FRM II reactor in the end of 2025.

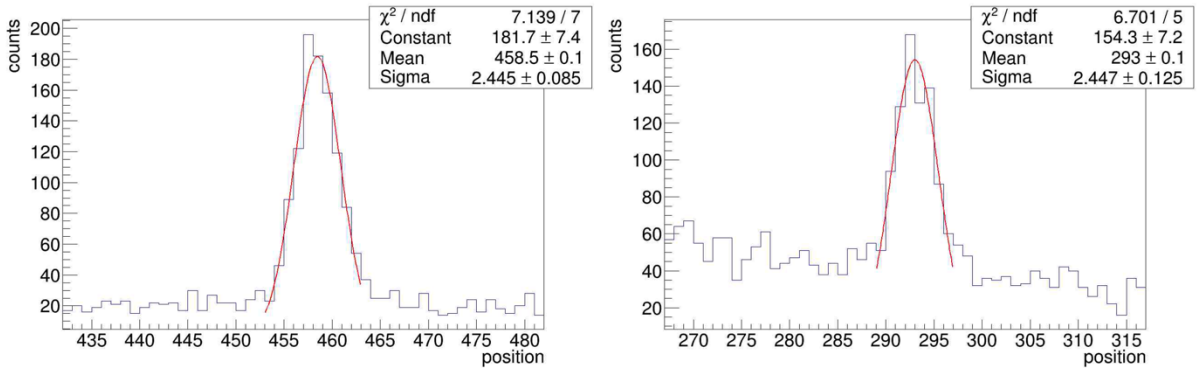


**Figure 14** Gaussian fit of the peaks detected during irradiation with neutrons from the $^{252}$Cf source along a $^{3}$He tube covered with an absorbing mask with local slits (2 mm width) across the tube: the left peak corresponds to the slit in the center of the tube, while the right peak originates from the slit at the left end of the tube. The FWHM = $2\sqrt{2\,ln2}$ Sigma is an indicator of the position resolution of the $^{3}$He tube along the tube axis.

## 1. Conclusions

New upgrades recently completed or in the process of being installed at the JCNS KWS-2 SANS diffractometer at MLZ are reported. These are specific upgrades to the sample environment and detection capabilities to enhance the performance of the instrument for selected scientific purposes in biology and energy applications. An in-situ SEC complimentarity has been optimized for the specific configuration at KWS-2 with the FPLC outside the sample area, to provide the instrument with biological samples of similar quality to other SAXS and SANS beamlines with SEC purification in the beam. For controlled in-beam hydration of solid ionomers or biological membranes, a versatile dew point generator dedicated to neutron scattering was calibrated and commissioned with Nafion membranes of known ionic conductivity measured with a variable RH and temperature conductivity cell. To bridge the atomic and mesoscale at KWS-2, a WANS option with a $^{3}$He tube detector is under construction, for which a quality assessment with a $^{252}$Cf neutron source was carried out at JCNS and FRM II. With a $Q_{max}$ = 2.0 Å$^{-1}$ and an adjustable resolution provided by the instrument's chopper in TOF mode, semi-crystalline materials or small biological morphologies can be structurally characterized in a very thorough way at the same beamline. All these innovations at KWS-2 will be fully operational when the FRM II reactor is brought back into operation, which is planned for the end of 2025. The planned restart of the reactor with only thermal neutrons in the first phase due to the delayed production of the new cold source will not have a severe impact on the new upgrades at KWS-2, although a lower operating flux than in the standard configuration is expected. A combined strategy is planned at KWS-2 to overcome the flux reduction caused by this temporary reactor configuration: (i) an increased use of shorter wavelengths around 3 Å, less affected by the absence of a cold source, while using a relaxed resolution with a dedicated velocity selector for $\Delta\lambda/\lambda \geq 20\%$; (ii) the repetition of measurements in the mid and high Q range to obtain good data statistics, which is a typical approach for SEC-SANS experiments; (iii) the use of neutron lenses and large sample sizes (up to 5 cm diameter) that are easily achievable for gel, colloid, micellar or membrane samples, which allows the intensity on the sample to be increased by a factor of up to 10 while maintaining the resolution as for pinhole geometry, thus compensating for the flux decrease in low Q measurements.

**Acknowledgements** JK and AR thank Prof. Dr. Masaaki Sugyiama and Prof. Dr. Rintaro Inoue (both Kyoto University, Japan) for their useful advice and suggestions in optimizing the SEC

complementarity to a SAS beamline. AR thanks Dr. Anne Martel (ILL, Grenoble, France) for invaluable suggestions at the beginning of the SEC project at KWS-2. We sincerely thank Noryuki Hikida (Canon Electron Tubes & Devices Co., Ltd., Otawara, Japan), Akinori Yamaguchi and Mitsugu Matsuura (both Clear Pulse Co., Ltd., Tokyo, Japan) for assisting with the test of the $^{3}$He tubes detector prototype at JCNS and Toshikuni Nagaya (TEKHNE Corporation, Kawasaki City, Japan) and Masao Ogura, Hideo Takashina and Takaaki Fukuda (all MicroEquipment Inc., Tokyo, Japan) for providing technical help during the commissioning of the humidity generator at JCNS. Warm thanks go to Toshiaki Morikawa (CROSS) for installing the precise dew point generator and humidity/conductivity system at TAIKAN, to Herbert Feilbach and Andreas Thelen (both Forschungszentrum Jülich GmbH) for help with the design of the WANS option at KWS-2, and to Dr. Karl Zeitelhack (Technical University of Munich) for the help during the test of the WANS detector with the $^{252}$Cf neutron source. The SANS experiment at the Materials and Life Science Experimental Facility of J-PARC was performed under a user program (proposal No. 2024C0006).

**Conflicts of interest** There are no conflicts of interest.

**Data availability** The data supporting the results reported in this article can be accessed upon request form the corresponding author.

## References

Adamski, M.; Peressin, N. & Holdcroft, S. (2021) *Mater. Adv*. 2, 4966-5005.

Akpalu, Y. V. (2010). *Polym. Rev*. 50, 1–13.

Allahyarov, E. & Taylor, P. L. (2009) *J. Phys. Chem.* B 113, 610-617.

Allen, A. J. (2023) *J. Appl. Cryst*. 56, 787-800.

Amann, M.; Willner, L.; Stellbrink, J.; Radulescu, A. & Richter, D. (2015) *Soft Matter* 11, 4208-4217.

Arima-Osonoi, H.; Takata, S.; Kasai, S.; Ohuchi, K.; Morikawa, T.; Miyata, N.; Miyazaki, T.; Aoki, H.; Iwase, H.; Hiroi, K.; Ogura, M.; Kikuchi, T.; Takashina, H. & Sakayori, T. (2023) *J. Appl. Cryst*. 56, 1802-1812.

Balacescu, L; Brandl, G. & Radulescu, A. (2021) *J. Appl. Cryst.* 54, 1217-1224.

Biehl, R. (2019) *PLoS ONE* 14, e0218789.

Bose, S.; Kuila, T.; Nguyen, T. X. H.; Kim, N. H.; Lau, K. & Lee, J. H. (2011) *Prog. Polym. Sci*. 36, 813-843.

Bucciarelli, S., Midtgaard, S. R., Nors Pedersen, M., Skou, S., Arleth, L. & Vestergaard, B. (2018). *J. Appl. Cryst.* **51**, 1623-1632.

Dewhurst, C. D.; Grillo, I.; Honecker, D.; Bonnaud, M.; Jacques, M.; Amroubi, C.; Perillo-Marcone, A.; Manzin, G. & Cubitt, R. (2016) *J. Appl.Cryst.* 49, 1-14.

Graewert, M. A., Da Vela, S., Gräwert, T. W., Molodenskiy, D. S., Blanchet, C. E., Svergun, D. I. & Jeffries, C. M. (2020). *Crystals* **10**, 975.

Grudinin, S.; Garkavenko, M. & Kazennov, A. (2017) *Acta Cryst*., D73, 449-464.

Grzybek, P.; Dudek, G. & van der Bruggen, B. (2024) *Chem. Eng. J.* 495, 153500.

Hammouda, B. (2010) *J. Appl. Cryst.* 43, 1474-1478.

Heenan, R. K.; King, S. M.; Turner, D. S. & Treadgold, J. R. (2005) *Proc. ICANS –* XVII, 780–785.

Heller, W. T.; Cuneo, M.; Debeer-Schmitt, L.; Do, C.; He, L.; Heroux, L.; Littrell, K.; Pingali, S. V.; Qian, S.; Stanley, C.; Urban, V. S.; Wu, B. & Bras, W. (2018) *J. Appl. Cryst*. 51, 242-248.

Houston, J. E.; Brandl, G.; Drochner, M.; Kemmerling, G.; Engles, R.; Papagiannopoulos, A.; Sarter, M.; Stadler, A. & Radulescu, A. (2018) *J. Appl. Cryst*. 51, 323-336.

Inoue, R., Nakagawa, T., Morishima, K., Sato, N., Okuda, A., Urade, R., Yogo, R., Yanaka, S., Yagi-Utsumi, M., Kato, K., Omoto, K., Ito, K. & Sugiyama, M. (2019). *Sci. Rep.* **9**, 12610.

Johansen, N. T., Pedersen, M. C., Porcar, L., Martel, A. & Arleth, L. (2018). *Acta Crystallographica* D **74**, 1178-1191.

Jordan, A., Jacques, M., Merrick, C., Devos, J., Forsyth, V. T., Porcar, L. & Martel, A. (2016). *J. Appl. Cryst.* **49**, 2015-2020.

Kanaya, T.; Matsuba, G.; Ogino, Y.; Nishida, K.; Shimizu, H. M.; Shinohara, T.; Oku, T.; Suzuki, J. & Otomo, T. (2007) *Macromolecules* 40, 3650-3654.

Kaneko, F.; Schiavone, M. M.; Iwase, H.; Takata, S.; Allgaier, J. & Radulescu, A. (2024) *Polymer* 295, 126771.

Klein, M.; Perrin, J.-C.; Leclerc, S.; Guendouz, L.; Dillet, J. & Lottin, O. (2013) *Diffusion Fundamentals* 18, 1-4.

Koizumi, S.; Noda, Y.; Maeda, T.; Inada, T.; Ueda, S.; Fujisawa, T.; Izunome, H.; Robinson, R. A. & Frielinghaus, H. (2020) *QuBS* 4, 42.

Krugmann, B.; Radulescu, A.; Appavou, M.-S.; Koutsioubas, A.; Stangaciu, L. R.; Dulle, M.; Förster, S. & Stadler, A. (2020) *Sci. Rep*. 10, 16691.

Kumada, T.; Motokawa, R.; Oba, Y.; Nakagawa, H.; Sekine, Y.; Micheau, C.; Ueda, Y.; Sugita, T.; Birumachi, A.; Sasaki, M.; Hiroi, K. & Iwase, H. (2023) *J. Appl. Cryst*. 56, 1776-1783.

Luo, X.; Rojas-Carbonell, S.; Yan, Y. & Kusoglu, A. (2020) *J. Membrane Sci*. 598, 117680.

Martel, A., Cocho, C., Caporaletti, F., Jacques, M., El Aazzouzi, A., Lapeyre, F. & Porcar, L. (2023). *J. Appl. Cryst.* **56**, 994-1001.

Mendil-Jakani, H.; Pouget, S.; Gebel, G. & Pintauro, P.N. (2015) *Polymer* 63, 99-107.

Monkenbusch, M.; Stadler, A.; Biehl, R.; Olivier, J.; Zamponi, M. & Richter, D. (2015) *J. Chem. Phys.* 143, 075101.

Noda, Y.; Koizumi, S. & Yamaguchi, D. (2016) *J. Appl. Cryst*. 49, 128-138.

Pabst, F.; Kraus, J.; Kloth, S.; Steinrücken, E.; Kruteva, M.; Radulescu, A.; Vogel, M. & Blochowicz, T. (2021) *J. Chem. Phys*. 155, 174501.

Pace, C. N., Vajdos, F., Fee, L., Grimsley, G. & Gray, T. (1995). *Protein Sci* **4**, 2411-2423.

Park, J. K.; Li, J.; Divoux, G. M.; Madsen, L. A. & Moore, R. (2011) *Macromolecules* 44, 5701-5710.

Pauw, B. R.; Smith, A. J.; Snow, T.; Shebanova, O.; Sutter, J. P.; Ilavsky, J.; Hermida-Merino, D.; Smales, G. N.; Terrill, N. J.; Thuenemann, A. F. & Bras, W. (2021) *J. Synchrotron Rad*. 28, 1-10.

Pedersen, J.S.; Posselt, D. & Mortensen, K. (1990) *J. Appl. Cryst*. 23, 321-333.

Puig-Rigall, J; Blanco-Prieto, M. J.; Radulescu, A.; Dreiss, C. A. & Gonzalez-Gaitano, G. (2021) *J. Coll. Interface Sci*. 582, 353-363.

Puig-Rigall, J.; Fernandez-Rubio, C.; Gonzalez-Benito, J.; Houston, J. E.; Radulescu, A.; Nguewa, P. & Gonzalez-Gaitano, G. (2020) *Int. J. Pharmaceutics* 578, 119057.

Radulescu, A., Pipich, V., Frielinghaus, H. & Appavou, M. S. (2012a). *J. Phys. Conf. Ser*. 351, 012026.

Radulescu, A., Pipich, V. & Ioffe, A. (2012b) *Nucl. Instrum. Methods Phys. Res. Sect.* A, 689, 1–6.

Radulescu, A., Szekely, N., Polachowski, S., Leyendecker, M., Amann, M., Buitenhuis, J., Drochner, M., Engels, R., Hanslik, R., Kemmerling, G., Lindner, P., Papagiannopoulos, A., Pipich, V., Willner, L., Frielinghaus, H. & Richter, D. (2015a) *J. Appl. Cryst*. 48, 1849-1859.

Radulescu; A., Goerigk; G., Fetters; L. & Richter, D. (2015b) *J. Appl. Cryst*. 48, 1860–1869.

Radulescu, A.; Arend, N.; Drochner, M.; Ioffe, A.; Kemmerling, G.; Ossovyi, V.; Staringer, S.; Vehres, G.; McKinny, K.; Olechnowicz, B. & Yen, D. (2016) J. Phys.: Conf. Ser. 746, 012026.

Radulescu, A. (2024) *J. Appl. Cryst*. 57, 1040-1046.

Rubatat, L. & Diat, O. (2007) *Macromolecules* 40, 9455-9462.

Ryan, T. M., Trewhella, J., Murphy, J. M., Keown, J. R., Casey, L., Pearce, F. G., Goldstone, D. C., Chen, K., Luo, Z., Kobe, B., McDevitt, C. A., Watkin, S. A., Hawley, A. M., Mudie, S. T., Samardzic Boban, V. & Kirby, N. (2018). *J. Appl. Cryst.* **51**, 97-111.

Schiavone, M-M.; Lamparelli, D.H.; Daniel, C.; Golla, M.; Zhao, Y.; Iwase, H.; Arima-Osonoi, H.; Takata, S.; Szentmiklosi, L.; Maroti, B.; Allgaier, J. & Radulescu, A. (2023) *J. Appl. Cryst*. 56, 947-960.

Takata, S.; Suzuki, J.; Shinohara, T.; Oku, T.; Tominaga, T.; Ohishi, K.; Iwase, H.; Nakatani, T.; Inamura, Y.; Ito, T.; Suzuya, K.; Aizawa, K.; Arai, M.; Otomo, T. & Sugiyama, M. (2015) *JPS Conf. Proc.* 8, 036020.

Shih, O., Liao, K.-F., Yeh, Y.-Q., Su, C.-J., Wang, C.-A., Chang, J.-W., Wu, W.-R., Liang, C.-C., Lin, C.-Y., Lee, T.-H., Chang, C.-H., Chiang, L.-C., Chang, C.-F., Liu, D.-G., Lee, M.-H., Liu, C.-Y., Hsu, T.-W., Mansel, B., Ho, M.-C., Shu, C.-Y., Lee, F., Yen, E., Lin, T.-C. & Jeng, U. (2022). *J. Appl. Cryst.* **55**, 340-352.

Sokolova, A.; Whitten, A.E.; de Campo, L.; Christoforidis, J.; Eltobaji, A.; Barnes, J.; Darmann, F. & Berry A. (2019) *J. Appl. Cryst.* 52, 1-12.

Sone, Y.; Ekdunge, P. & Simonsson, D. (1996) *J. Electrochem. Soc*. 143, 1254-1259.
Song, H.; Liu, Y.; Zhang, W.; Zhang, X.; Yin, X.; Li, J. & Wu, G. (2022) *J. Power Sources* 539, 231623.
Talley, S. J.; Vivod, S. L.; Nguyen, G. A.; Meador, M. A. B.; Radulescu, A. & Moore, R. B. (2019) *ACS Appl. Mater. Interfaces* 11, 31508-31519.
Tashiro, K. & Sasaki, S. (2003) *Polymer* 28, 451-519.
Thureau, A., Roblin, P. & Pérez, J. (2021). *J. Appl. Cryst.* **54**, 1698-1710.
Wang, H.; Holmberg, B. A.; Huang, L.; Wang, Z.; Mitra, A.; Norbeck, J. M. & Yan, Y. (2002) *J. Mater. Chem.* 12, 834-837.
Yoshimura, K.; Hiroki, A.; Radulescu, A.; Noda, Y.; Koizumi, S.; Zhao, Y. & Maekawa, Y. (2024) *Macromolecules* 57, 1998-2007.
Zhao, Y.; Yoshimura, K.; Motegi, T.; Hiroki, A.; Radulescu, A. & Maekawa, Y. (2021) *Macromolecules* 54, 4128-4135.
Zhao, Y.; Yoshimura, K.; Sawada, S.; Motegi, T.; Hiroki, A.; Radulescu, A. & Maekawa, Y. (2022) *Macromolecules* 55, 7100-7109.
Zhao, J. K.; Gao, C. Y. & Liu, D. (2010) *J. Appl. Cryst*. 43, 1068–1077.

# Supporting information

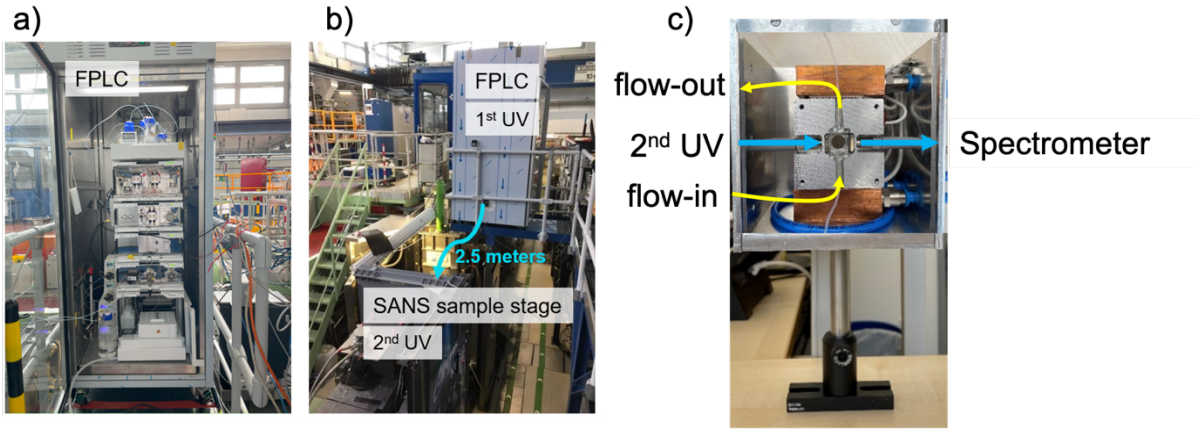


**Figure S1** Pictures of different parts of the SEC-SANS setup at the KWS-2 instrument at MLZ. (a) The FPLC instrument in a fridge. (b) The spatial arrangement: the FPLC instrument is located at an elevated platform above the SANS sample stage. (c) The SANS cuvette holder that comes on the sample stage: the yellow arrows indicate the sample flowing through the customized quartz cuvette while the blue arrows shows the UV beam direction. The temperature on the cell can be varied in a controlled way by using the Peltier elements mounted between the Al-holder and the copper oven (with water cooling).

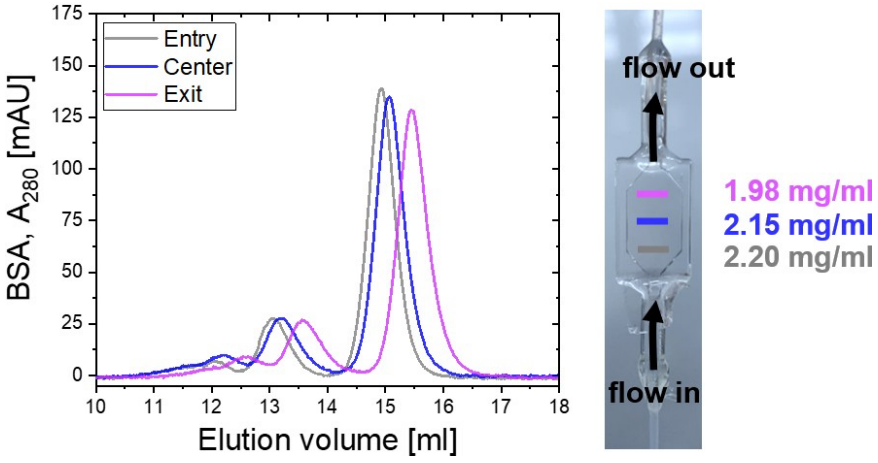


**Figure S2** Elution profiles of 10 mg/ml bovine serum albumin, BSA, when the 2nd UV detects at the front window of the flow cell at different positions as indicated, with the corresponding protein concentration written aside.


**Figure S3** The precise dew point generator with two reservoirs for in-situ changing the contrast in the sample by providing vapor of either H2O, D2O or any H2O/D2O combination (left) and the multiposition sample chamber that works together with the generator. The dew point mirror sensor setup is visible in top of the chamber. Photos are taken during the calibration test carried out at JCNS.

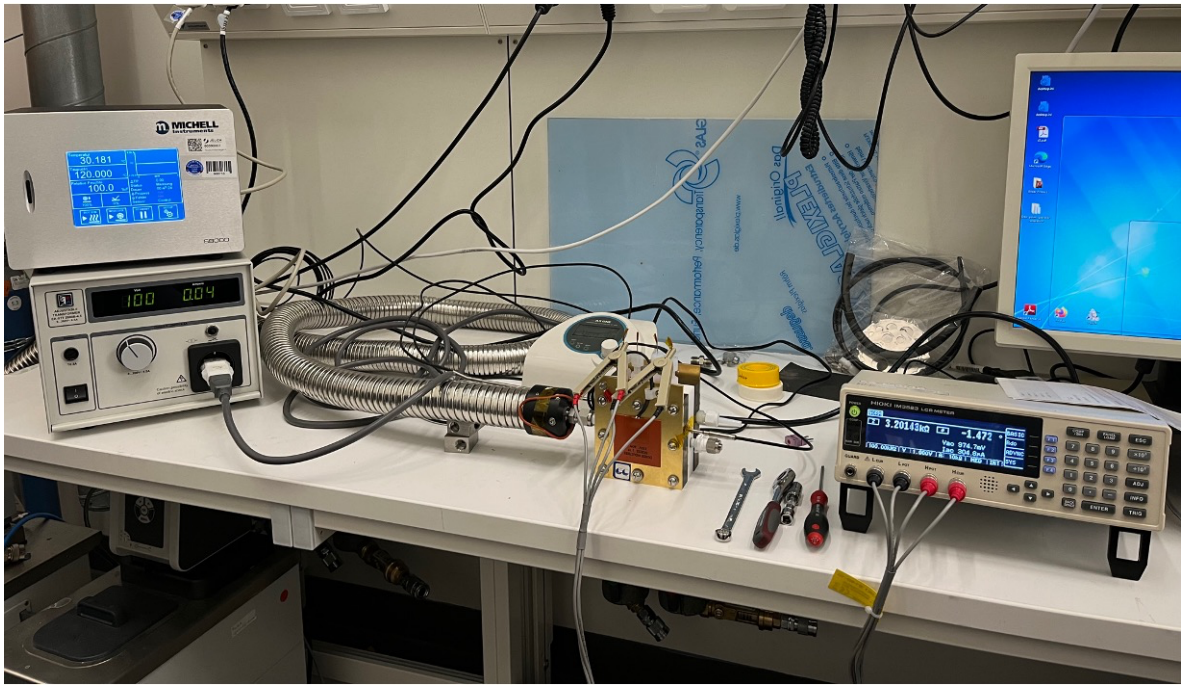


**Figure S4** Experimental arrangement at JCNS for measuring the conductivity on the Nafion membranes in variable RH and T conditions. The conductivity cell (Electrochem Inc.) is the yellow device and it is fed with vapors from the dew point generator through the silver tubing coming from the left side. The temperature on the cell is varied by using the device on back side of the cell with the controller placed on the far left side. The LCR meter is the device on the far right side.

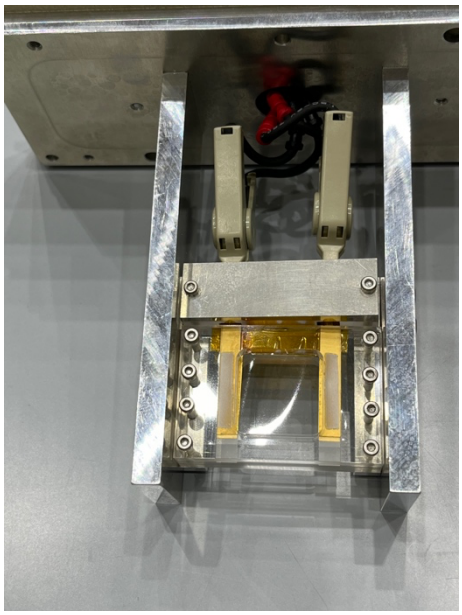

**Figure S5** The humidity/conductivity cell (inner elements) of BL-15 Taikan, J-PARC, for simultaneous use with SANS with an as-received Nafion film installed between the electrodes to be exposed to controlled relative humidity and temperature using a single-position humidity chamber.

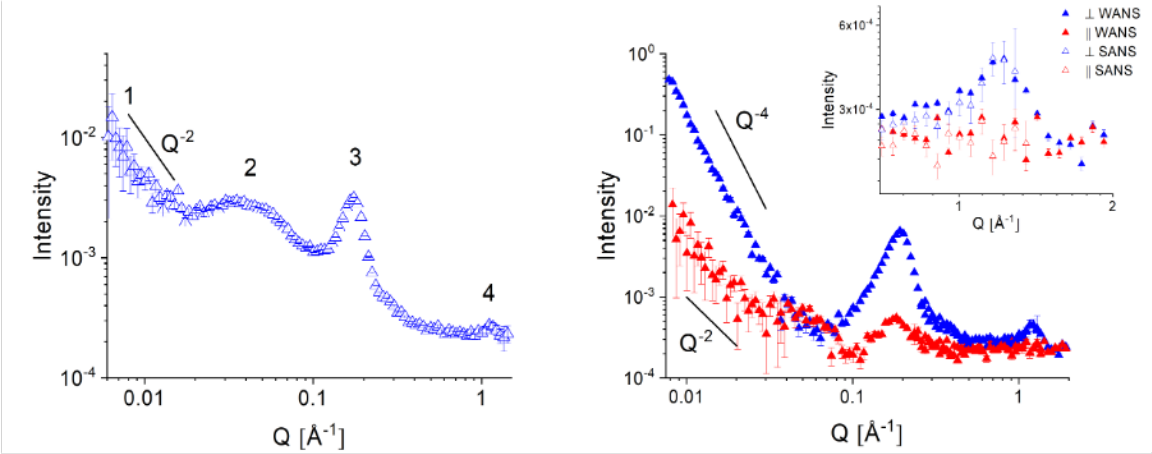


**Figure S6** SANS patterns from as received (left) and uni-axially deformed (right) Nafion membranes collected at 80 °C and RH = 85%. Discussion of the results can be found in the main text. The detailed work of simultaneous SANS and in-situ conductivity measurements on polymer electrolyte mebranes at different RH and T conditions will be reported in a forthcoming publication.

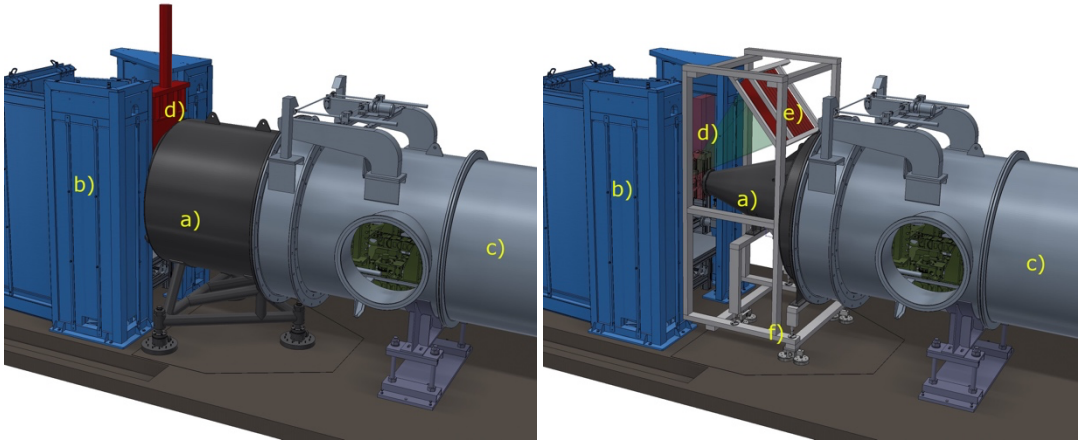


**Figure S7** Schematic representation of the KWS-2 components at the sample position and the detection elements at $L_D$ = 1.5-2 m after the sample. Left side - the old setup with a) the cylindrical first segment of the evacuated tank, b) the lead shield around the sample position, c) the rest of the evacuated tank and d) the vacuum shutter behind the entrance window. Right side - the current under construction setup: the new elements are d) the mechanical protection in front of the entrance window, which moves vertically in a controlled fashion and is interlocked with the access door to the sample position to protect the window from mechanical shocks when work is performed at the sample position, e) the WANS detection panel and f) the support frame of the WANS detection panel, which can be equipped with additional shielding elements.

**Figure S8** The $^{3}$He detector tubes array during the test with the $^{252}$Cf source at FRM II, MLZ Garching: the backside of the detector with the signal and power cables (left) and the front side (right).

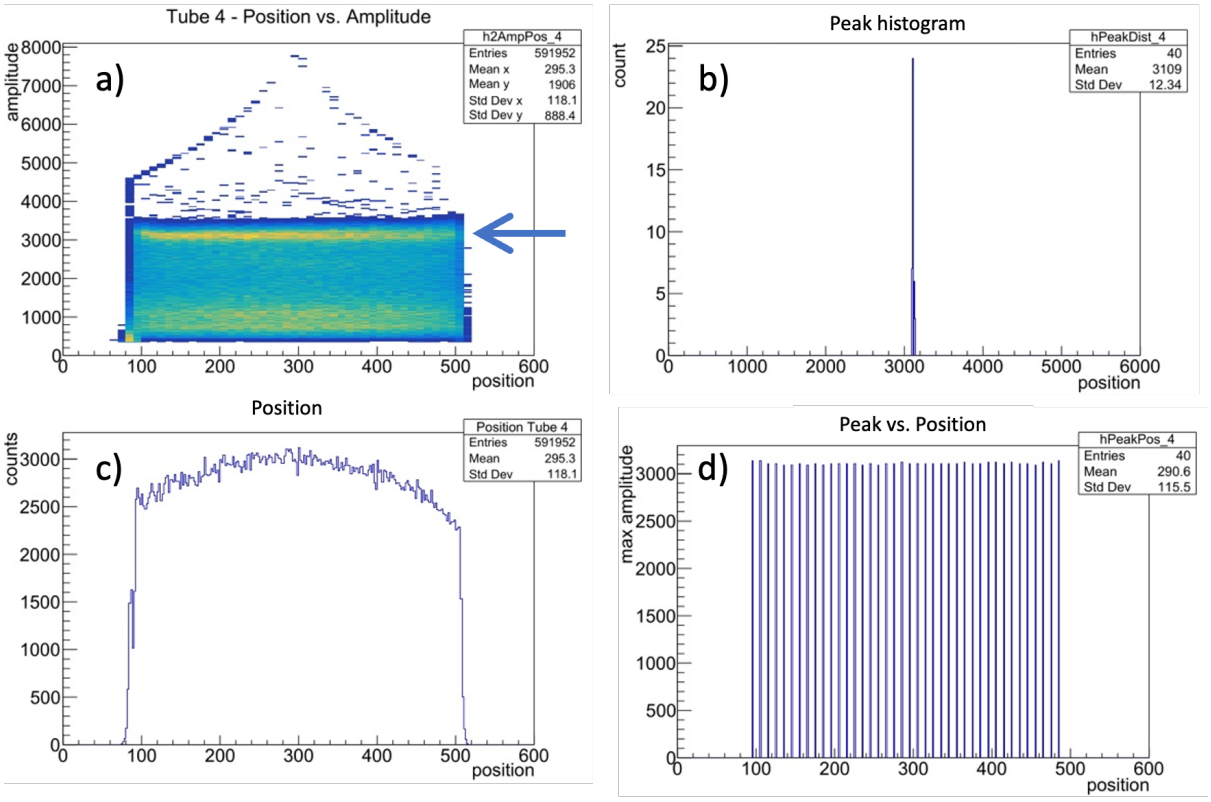


**Figure S9** Example of analysis of measured data with the detector: a) position vs. amplitude; b) neutron peak distribution (indicated by the arrow in a)); c) integrated intensity vs. position; d) neutron peak intensity vs. position. For all $^{3}$He tubes the neutron peak distribution was less than 5%.

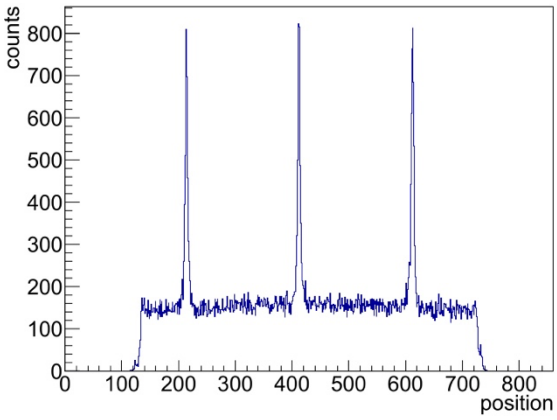


**Figure S10**Example of data measured on detector using the Cd-mask with three narrow slits (3 mm); the peaks may be used for the estimation of the detector resolution at different positions along the $^{3}$He tube.